Computational comparison of the conventional diesel and hydrogen direct-injection compression-ignition combustion engines

Fuel 307 (2022) 121909

Contents lists available at ScienceDirect

Fuel

journal homepage: www.elsevier.com/locate/fuel

Full Length Article

Computational comparison of the conventional diesel and hydrogen direct-injection compression-ignition combustion engines

Rafig Babayev [a,*], Arne Andersson [b], Albert Serra Dalmau [b], Hong G. Im [c], Bengt Johansson [a]

[a] Combustion Engine Research Center (CERC), Chalmers University of Technology, Sweden
[b] Powertrain Strategic Development (PSD), Volvo Group Trucks Technology (Volvo GTT), Sweden
[c] Clean Combustion Research Center (CCRC), King Abdullah University of Science and Technology (KAUST), Saudi Arabia

ARTICLE INFO

Keywords:
Hydrogen combustion
Diesel combustion
Direct injection
Compression ignition
Hydrogen engine
CFD

ABSTRACT

Most research and development on hydrogen (H_2) internal combustion engines focus on premixed-charge spark ignition (SI) or diesel-hydrogen dual-fuel technologies. Premixed charge limits the engine efficiency, power density, and safety, while diesel injections give rise to CO_2 and particulate emissions. This paper demonstrates a non-premixed compression-ignition (CI) neat H_2 engine concept that uses H_2 pilots for ignition. It compares the CI H_2 engine to an equivalent diesel engine to draw fundamental insights about the mixing and combustion processes. The Converge computational fluid dynamics solver is used for all simulations. The results show that the brake thermal efficiency of the CI H_2 engine is comparable or higher than diesel, and the molar expansion with H_2 injections at TDC constitutes 5–10 % of the total useful work. Fuel-air mixing in the free-jet phase of combustion is substantially higher with H_2 due to hydrogen's gaseous state, low density, high injection velocity, and transient vortices, which contribute to the 3 times higher air entrainment into the quasi-steady-state jet regions. However, the H_2 jet momentum is up to 4 times lower than for diesel, which leads to not only ineffective momentum-driven global mixing but also reduced heat transfer losses with H_2. The short H_2 flame quenching distance may also be inconsequential for heat transfer in CI engines. Finally, this research enables future improvements in CI H_2 engine efficiency by hypothesizing a new optimization path, which maximizes the free-jet phase of combustion, hence is totally different from that for conventional diesel engines.

1. Introduction

In the context of the European Green Deal [1], in 2020, the EU has announced plans of drastic expansion of hydrogen (H_2) infrastructures and large-scale deployment of H_2 technologies [2–4] across multiple sectors, including transportation. This sparked a tremendous interest in hydrogen as a potentially carbon–neutral energy carrier for the mobility sector. It attracted extra attention in energy-intensive applications such as heavy-duty and long-range transport, where alternatives, such as battery-electric technology, are less feasible. Thus, energy conversion devices that are capable of direct use of H_2, such as fuel cells and internal combustion engines (ICE), are expected to become widely used in the near future. This work focuses on the latter technology.

Certain types of hydrogen ICEs are extensively studied, such as spark ignition (SI) and homogeneous charge compression ignition (HCCI) [5–11], as well as dual-fuel engines [12–15]. On the other hand, research on the compression-ignition (CI) nonpremixed H_2 combustion engines is currently very limited, despite many advantages that this concept offers compared to the premixed combustion alternatives. The potential advantages of the nonpremixed approach are elaborated in Section 2. The scarcity of research on neat H_2 nonpremixed CI combustion is explained by the following:

1. The high auto-ignition temperature of hydrogen (585 versus 250 ℃ for H_2 and diesel, respectively [16]) and a research octane number (RON) above 130 [17] typically result in the need for either higher than normal compression ratios, or elevated inlet temperatures to achieve CI combustion. The former is challenging due to increased thermal and mechanical loads on the engine, and the latter commonly leads to lower volumetric efficiency, elevated heat losses, and excessive NOx emissions.
2. The need for the injection system pressure considerably higher than the peak in-cylinder pressure at all times to guarantee fuel flow from the injector to the cylinder. To our knowledge, there were no

* Corresponding author at: Division of Combustion and Propulsion Systems, Hörsalsvägen 7B, SE-412 96, Göteborg, Sweden.
E-mail address: rafig@chalmers.se (R. Babayev).

https://doi.org/10.1016/j.fuel.2021.121909
Received 13 May 2021; Received in revised form 11 August 2021; Accepted 2 September 2021
Available online 9 September 2021

Definitions/Abbreviations

$\overline{TKE}_{react}$	average turbulence kinetic energy of the reaction region
y^+	dimensionless inner distance
φ_R	reaction equivalence ratio
AMR	adaptive mesh refinement
ASOMI	after start of main injection
ASOPI	after start of pilot injection
ATDC	after top dead center
BTE	brake thermal efficiency
CA°	crank angle degree
CA50	crank angle of 50% heat release
CA90	crank angle of 90% heat release
CDC	conventional diesel combustion
CFD	computational fluid dynamics
CFL	Courant–Friedrichs–Lewy
CI	compression ignition
CNG	compressed natural gas
DCEE	double compression-expansion engine
DI	direct injection
EGR	exhaust gas recirculation
EOI	end of injection
FJM HR%	percentage of the heat release in the free-jet mixing phase
FuelMEP	fuel mean effective pressure
GIE	gross indicated efficiency
GIW	gross indicated work on the piston
HT	heat transfer
ICE	internal combustion engine
$IMEP_{gross}$	gross indicated mean effective pressure
IVC	inlet valve closing
LHV	lower heating value
N	number of moles
P	pressure
PCP	peak cylinder pressure
PFI	port fuel injection
PMP	peak motoring pressure
RANS	Reynolds-averaged Navier Stokes
RoHR	rate of heat release
RON	research octane number
RPM	revolutions per minute
SI	spark ignition
TDC	top dead center
η	number of atoms
λ	air-fuel equivalence ratio

commercially available hydrogen fuel injectors that could fulfill the requirements of modern high-performance diesel engines.

Lean stratified charge combustion (SCC) is another promising technology for H_2 engines [18–21], which may reduce NOx emissions compared to the CI mode. However, it is currently less suitable for heavy-duty applications, especially in the context of double compression-expansions engines (see below), owing to the extremely high levels of air dilution, hence limited power density. Furthermore, optimized CI H_2 engines may offer comparable improvements in heat transfer losses (see Section 5.5) to the SCC, while allowing higher equivalence ratios, hence higher efficiency.

Ikegami et al. [22] were among the first to achieve successful CI H_2 engine operation, even though they faced issues with ignition and achieving higher engine loads. Similar problems were reported by Furuhama et al. [23] in a two-stroke engine, thus a spark plug was used for ignition. Naber et al. [24] used a constant-volume chamber to investigate nonpremixed H_2 combustion at conditions approaching diesel engines. Despite being able to showcase this technology's feasibility, they did not implement it in an actual engine. Eichlseder et al. [25] achieved CI H_2 combustion with a help of a lean premixed charge ignited by a spark plug, while Kavtaradze et al. [26–28] and Rottengruber et al. [16] focused mainly on the NOx emission characteristics. The latter research group also studied CI H_2 engines computationally but reported a phenomenon that resembled premixed flame propagation. They described this phenomenon as a "combustion wave" and attributed it to the high diffusivity of hydrogen.

To this end, our previous work [29] was the first to provide a detailed computational characterization of a truly nonpremixed neat H_2 combustion concept. It focused on the computational fluid dynamics (CFD) modeling of DICI H_2 combustion engines by employing numerical methods that reproduce the direct H_2 injection process at optimal accuracy and computational efficiency. Model validation against optical constant-volume chamber and diesel engine experimental data was performed, and characterization of the nonpremixed H_2 combustion cycle was carried out in terms of the heat release trace. This was realized in the context of a modern CI engine concept, the double compression-expansion engine (DCEE).

The DCEE consists of three dedicated cylinders: compressor, combustor, and expander, and promises large efficiency improvements at low cost [30–33]. The compressor cylinder enables higher boost and EGR levels, while the expander cylinder uses the exhaust gases from the combustion cylinder to extract additional useful work. The issue of high autoignition temperature of H_2 may be solved by the DCEE as it allows higher inlet temperatures for the combustion cylinder without significant repercussions on efficiency and emissions, owing to the more degrees of freedom that the concept allows for optimization [30–34].

It was also demonstrated in [29] that H_2 jets and mixing differ substantially from those with diesel fuel. H_2 jets exhibited weak air entrainment *near the injector nozzle*, hence no premixing was observed. Unlike with diesel, combustion in H_2-fueled CI engines is driven both by free turbulent jet mixing and global in-cylinder mixing, and the heat release is much faster in the former mode. However, the underlying physical phenomena behind the reported observations, including the flow structures generated by the H_2 jets, were not discussed due to the lack of understanding. No detailed comparison was made between diesel and H_2 CI engines, which is crucial for engine development. Also, the expected energy losses in DICI H_2 engines have not been explored before.

The current work is a logical continuation of our previous study, aiming to explain the previous findings, compare the diesel and DICI H_2 combustion engines in great detail, thus drawing fundamental insights about fuel–air mixing, combustion, and energy losses, and make recommendations for future engine optimization. It starts with a parametric analysis of the nonpremixed H_2 combustion approach versus the premixed one, motivating opting for the former (Section 2). Then, it describes the employed numerical models (Section 3) and experimental setup and operating conditions (Section 4). The study then aims to characterize the proposed pilot ignition strategy (Section 5.1) and compares the DICI H_2 and diesel combustion cycles (Section 5.2). The work then focuses on understanding the phenomena behind the drastically larger proportion of the free-jet mixing mode with H_2 combustion, as well as the faster burning rate in the corresponding phase of the engine cycle (Section 5.3), and investigates the vortical structures generated by the H_2 jets (Section 5.3.2). Finally, the sources of useful work loss in DICI H_2 engines, especially wall heat transfer, are explored (Section 5.4), and practical implications for engine development are made (Section 5.5). All crucial findings are summarized in Section 6.

2. Premixed versus nonpremixed hydrogen combustion engines

As mentioned in Section 1, the nonpremixed CI H_2 combustion concept has many advantages over the premixed (SI, HCCI, etc.) approaches, which are too attractive to be ignored. These include (1) the eliminated risk of knock and pre-ignition, (2) higher thermal efficiency, (3) higher power density compared to the PFI concepts where hydrogen displaces air in the intake, (4) no risk of backfiring into the intake manifold, (5) potentially lower cycle-to-cycle variability, (6) the absence of combustible gases in the crankcase, which is especially relevant considering hydrogen's wide ignitibility limits, (7) net molar expansion, and (8) reduced work input during the compression stroke. The first five points have been addressed by other authors [28,35,36]. The sixth point is self-explanatory. The last two points are further elaborated on here.

Fig. 1 (A) shows the total number of moles in the cylinder as a function of crank angle for the conventional diesel and hydrogen engines. The stoichiometric oxidation reaction of n-heptane and air has a molar expansion ratio of 1.056 [37], which is manifested in the gradual rise in the total mole number for the diesel case in Fig. 1 (A) and contributes to the useful work on the piston. Note that the rise is smaller than the theoretical due to the different equivalence ratios. On the other hand, the molar expansion ratio for the stoichiometric oxidation reaction of hydrogen and air is below unity, at 0.852 [37]. This is manifested in the falling mole number after the initial rise due to the injection for the reacting H_2 case in Fig. 1 (A). However, for a fixed engine load (constant FuelMEP), the number of injected moles of hydrogen is around 30 times larger than that of diesel fuel. This is because H_2 has a very low molecular weight, 2 g/mole, as opposed to around 170 g/mole for a common diesel fuel [38], while the LHV of H_2 is 120 MJ/kg versus ~ 43 MJ/kg for diesel [39].

This is also another advantage of the CI H_2 approach over the PFI and DI *premixed* combustion operations with early injections because the latter would only see a reduction in the net in-cylinder mole number during the power stroke due to the H_2 combustion chemistry while spending more energy to compress the larger number of moles during the compression stroke. The molar expansion work gain by the H_2 injection at TDC is also illustrated by the P-V diagram in Fig. 1 (B), showing a significant area enclosed within the trace of the non-reacting TDC-injection case, which corresponds to an $IMEP_{gross}$ of around 2.4 bar, 9.7 % of total produced work or 4.1 % of the total fuel energy. Considering that the H_2 combustion reactions eliminate approximately half of the gains and that it occurs at a considerably slower rate than the addition of moles during injection (see Fig. 1, A), the molar expansion work generated in the actual combustion cycle would lie *between 2.1 and 4.1 % of the fuel energy, or 4.9 and 9.7 % of the total produced work*.

3. Numerical setup

The modeling approach used in this work is taken from our previous study [29], where it was carefully optimized for computational cost and accuracy, tested for grid independence, and validated against optical constant-volume chamber and all-metal engine experimental data.

All three-dimensional Reynolds-averaged Navier Stokes (RANS) simulations were performed using the CONVERGE CFD solver [40], with a structured cut-cell Cartesian grid. The turbulence was modeled using the RNG k-ε model with standard coefficients. For computational savings, the engine cylinder and injector nozzle geometries were divided into 7 sectors, each with one nozzle orifice. Periodic boundary conditions are imposed on the surfaces that connect the adjacent sectors, as illustrated in Fig. 2. The base computational grid resolution is 2 mm, with the injector nozzle and jet embedding of scale 4 (see Fig. 2) and adaptive mesh refinement (AMR) everywhere else in the computational domain of up to scale 3. The refinement criteria are temperature, velocity, and H_2 species mass fraction, with the subgrid threshold values of 0.1 m/s, 2.5 K, and 1E-4, respectively. The latter criterion is required owing to hydrogen's high diffusivity. The computational grid is also tilted along the *y* axis (see Fig. 2) making it aligned with the dominant flow direction, and thus allowing an easier grid convergence with improved solution accuracy.

Additional AMR of up to scale 4 is also employed on all near-boundary cells to keep the y^+ value within the recommended range (30 to 100). This enables the use of the wall function approach for wall heat transfer modeling, thus eliminating the need to resolve the computationally expensive viscous boundary layer. The heat transfer model used is the O'Rourke and Amsden model [41], given as:

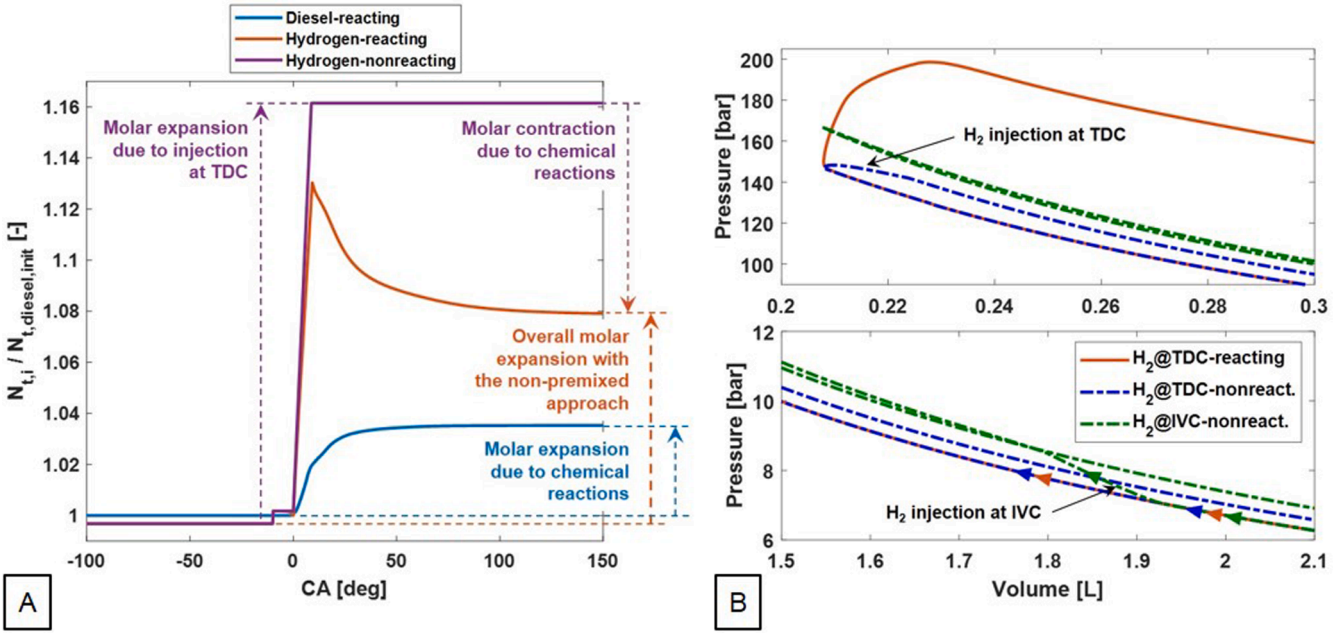

Fig. 1. (A) – Total number of moles in the cylinder as a function of crank angle for the conventional diesel and hydrogen engines, normalized by the initial mole number in the former. (B) – P-V diagram for the hydrogen engine with injections at IVC (premixed) and TDC (non-premixed) under the reacting and non-reacting conditions.

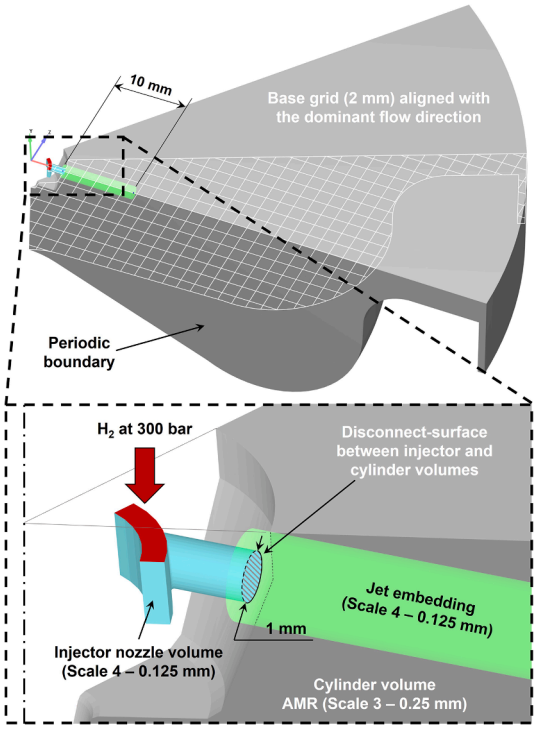

Fig. 2. The hydrogen injection simulation approach adopted in this study for DICI engines.

$$k\frac{\partial T}{\partial x} = \frac{\mu_m c_p \left(T_g - T_w\right)}{Pr_m y} F \tag{1}$$

$$F = 1.0y^+ < 11.05 \tag{2}$$

$$F = \frac{\frac{y^+ Pr_m}{Pr_t}}{\frac{1}{\kappa} lny^+ + B + 11.05\left(\frac{Pr_m}{Pr_t} - 1\right)} y^+ > 11.05 \tag{3}$$

$$y^+ = \frac{\rho u_\tau y}{\mu_m} \tag{4}$$

where y is absolute wall distance, y^+ is dimensionless wall distance, Pr_m is molecular Prandtl number, T_w is wall temperature, T_g is gas temperature, μ_m is molecular viscosity, k is molecular conductivity, Pr_t is turbulent Prandtl number, u_τ is shear speed, κ is Von Karman constant equal to 0.42, and B is law-of-the-wall parameter equal to 5.5.

The Redlich-Kwong-Soave (RKS) equation of state is used in conjunction with species-specific critical temperature, critical pressure, and acentric factor for accurate prediction of the Joule-Thomson effect with hydrogen [42]. To ensure that the solution for the species transport equations takes into account the characteristically low molecular Schmidt number of H_2, the solver calculates the mixture-averaged binary diffusion coefficients using a "transport.dat" file provided with the kinetic mechanism, which are subsequently used to estimate the local mixture-averaged and total diffusion coefficients [29,43]. This approach gave more accurate predictions compared to the singe-species diffusion Tautology, and similar results to a mixture-averaged diffusion with directly specified Schmidt number for each species. Furthermore, results with three different "transport.dat" files were also compared (including those from [44–46]) showing a good agreement.

The time integration is performed using a variable time-step algorithm with maximum convection, diffusion, and Mach CFL limits of 0.3, 2.0, and 50.0, respectively.

The simulation methodology of the H_2 fuel injection process involves modeling the injector nozzle volume with an imposed pressure-inflow boundary condition between the injector needle and its body, as illustrated in Fig. 2. The geometry is based on the HPDI natural gas injector [47], with seven *circular* nozzle orifices, each having a diameter of 1 mm and a channel length of approximately 2 mm. The surface disconnecting the injector and cylinder regions (striped disk) is removed during the injection process and put up again to stop the injection. The injection rate profile is assumed to be quasi-square while taking into account the effects of the varying in-cylinder pressure. This approach to direct hydrogen injections was validated before against experimental results from a constant-volume chamber equipped with a GDI injector fueled with H_2 [29].

The H_2 combustion process is modeled using the SAGE chemistry solver with a detailed high-pressure H_2 combustion kinetic mechanism by Burke et al., 2012 [48]. The kinetic model was designed to perform well with dilute and high-pressure flames and validated at the temperatures, pressures, and equivalence ratios of *298–3000 K, 0.3–87 atm, 0.25–5.00 (φ)*, respectively. It was further evaluated in [29] and found to perform well at the conditions of interest for the previous and this study.

For diesel combustion, a discrete phase Lagrangian model is used to simulate the injection of liquid diesel and its atomization. A total of 60,000 liquid parcels are added to the computational domain over the course of the injection, which bear the physical properties of diesel fuel. A KH-RT model without breakup length is used for spray atomization and breakup modeling. The Frossling model is then used to model the evaporation of the liquid parcels into n-C_7H_{16}. The diesel combustion reactions are modeled using an "AramcoMech" kinetic mechanism [49] for complex TPRF surrogate fuels (n-C_7H_{16} in this case) at high-pressure compression-ignition conditions. The model contains 61 species and 270 reactions.

Finally, all the models used in this study were validated in [29] against optical constant-volume chamber and all-metal diesel engine experimental data. For further details on the numerical setup and solution methods, also refer to [29].

4. Experimental setup and operating conditions

The boundary conditions used in the engine rig tests by Lam et al. [32] were adopted in this work to simulate both the conventional diesel combustion (CDC) and DICI H_2 engines. The test rig was based on a single-cylinder variant of a standard heavy-duty Volvo D13 diesel engine. The engine used a low compression ratio piston (CR = 11.5:1) and moderately pressurized inlet and exhaust to replicate the DCEE combustor unit operation. Table 1 reports the test rig specifications and operating conditions. One CDC cycle is considered for validation, whereas the other for comparison with the DICI H_2 combustion cycle. The operating conditions for the former match the experimental data, while those for the latter are slightly modified for a better comparison. The modifications include increased temperature and pressure at IVC, and thus also a slightly changed composition of the gas. The pressure and temperature are increased to match the TDC conditions from the DICI H_2 case, which in turn, required it for easier ignition. However, the required increase is smaller than that reported in [16], for example, owing to the H_2 pilot injection strategy proposed in this work (for details, see Section 5.1).

Also note that, for the sake of comparison, the peak motoring pressure (PMP), peak cylinder pressure after combustion (PCP), global air–fuel equivalence ratio (λ), and fuel mean effective pressure (FuelMEP) are set equal in the CDC (comparison) and DICI H_2 cases. The injection timing, IVC in-cylinder pressure, and EGR rate were adjusted. The injected fuel mass was also changed due to the different LHV values of diesel and H_2.

One important assumption is the identical wall temperatures in the CDC and DICI H_2 combustion simulations. This decision is justified by the fact that wall temperatures are typically set in a way to avoid premature thermal degradation of the combustion chamber materials.

Table 1
Research engine rig specifications and operating conditions for the CDC and DICI H_2 combustion cases.

	CDC (validation)	CDC (comparison)	DICI H_2 combustion
Cylinder bore	131 mm		
Stroke	158 mm		
Con. Rod length	267.5 mm		
Compression ratio	11.5:1		
In-cylinder pressure at IVC *	6.8 bar	7.1 bar	7.0 bar
In-cylinder temperature at IVC *	173 °C	255 °C	255 °C
Pilot injection fuel mass	–	–	1.5 mg
Pilot injection timing	–	–	−10 CA° ATDC
Pilot injection duration	–	–	0.5 CA°
Main injection fuel mass	275.6 mg	275.6 mg	99.5 mg
Main injection timing	−3 CA° ATDC	−3 CA° ATDC	0 CA° ATDC
Main injection duration	10.8 CA°	10.8 CA°	9.4 CA°
Number of nozzle orifices	7	7	7
Orifice diameter	0.265 mm	0.265 mm	1 mm
Spray umbrella angle	145°	145°	132°
Injection pressure (main and pilot)	2200 bar	2200 bar	300 bar
FuelMEP	56.9 bar	56.9 bar	56.9 bar
Engine speed	1200 RPM	1200 RPM	1200 RPM
Global air–fuel equivalence ratio (λ)	1.36	1.17	1.17
EGR rate	40 %	40 %	48 %
Piston temperature	527 °C	527 °C	527 °C
Cylinder liner temperature	337 °C	337 °C	337 °C
Cylinder head temperature	467 °C	467 °C	467 °C
	In-cylinder composition at IVC (mass fractions)		
H_2O	0.0325	0.0307	0.0966
N_2	0.7416	0.7478	0.7762
O_2	0.1563	0.1413	0.1272
CO_2	0.0696	0.0803	–

Hence, even if the heat flux to the cylinder walls is lower with the DICI H_2 combustion cycle, the wall temperatures would stay largely unchanged because of a reduced cooling rate that would be implemented with efficiency considerations in mind.

5. Results and discussion

5.1. Hydrogen-pilot-assisted compression ignition

Due to the requirement of an ideally CO_2-free engine, previously implemented ignition strategies for high-octane fuels (such as CH_4), that utilize pilot diesel injections in DI CNG engines [50–53], cannot be used in the current engine concept. Instead, a single-fuel implementation is proposed, which uses the compression-ignition of a small pilot injection of H_2 for a subsequent ignition of the main hydrogen jet.

Owing to the high auto-ignition temperature of hydrogen, slightly higher TDC temperatures are required for this strategy to work. According to 0D ignition delay simulations, at the peak motoring temperature of the CDC (valid.) case of 1000 K, the ignition delay of the H_2 mixture with 48% EGR is between 10 and 30 CA° (as a lower limit). Hence, the TDC temperatures must be raised to achieve more reasonable ignition delay values. At 1130 K, the ignition delay of the H_2 mixture with 48% EGR is estimated to be in the range of 1–3 CA°, which is reasonable and is used for all subsequent DICI H_2 combustion cycle simulations. It offers reasonably high volumetric efficiency while still allowing deviations in the ignition delay arising from the temporal variations in the actual in-cylinder temperature. Modern engine concepts, such as the DCEE, can achieve higher inlet temperatures for the combustor unit without a significant penalty on the overall engine efficiency. Hence, the proposed single-fuel pilot-assisted ignition is a feasible strategy for such engines.

The following offers a description of the proposed strategy. The IVC temperature of the combustor unit is set at 528 K (see Table 1), which leads to ~ 1130 K at TDC. Then, a pilot injection of 1.5 mg (1–2 % of the main injection mass) of hydrogen is made at −10 CA° ATDC. The process of the pilot ignition starts as the plume gradually leans down and heats up, achieving thermal equilibrium with the surrounding gas, as illustrated in Fig. 3. Starting from −1 CA° ATDC, exothermic reactions, primarily occurring at φ of around 0.3–0.5, start rapidly heating the pilot plume. The reaction equivalence ratio is defined as:

$$\varphi_R = \frac{2\sum_i N_i \eta_{C,i} + \frac{1}{2}\sum_i N_i \eta_{H,i}}{\sum_i N_i \eta_{O,i}} \quad (5)$$

where N_i is the mole number of species i, and $\eta_{C,i}$, $\eta_{H,i}$ and $\eta_{O,i}$ are, respectively, the number of carbon, hydrogen, and oxygen atoms in species i. Note that CO_2 and H_2O (combustion products) are not considered here, hence the name "reaction equivalence ratio".

Fig. 3 shows that the entire inner part of the hydrogen plume, which was at φ_R of 0.3–0.5, reacts homogenously and reaches a temperature of around 1500–1600 K at TDC. The main injection also starts at TDC, immediately encounters the hot pilot plume, and ignites instantly. The flame propagates along the stoichiometric peripheries of the jet toward the nozzle, quickly releasing a large amount of heat (see Fig. 4), before a truly nonpremixed combustion is established. Since the pilot takes about 10 CA° to ignite, it is evident that without it, the main injection commenced at TDC would ignite too late. Further increasing the inlet temperature to achieve a reasonable ignition delay without the pilot would negatively affect engine efficiency.

The obtained results are consistent with experimental data by Eichlseder, et al. [25], in that the reliable autoignition of the H_2 pilot plumes and the subsequent ignition of the main injection are feasible at these temperatures. However, in their study, a much larger amount of fuel is burned in autoignition mode, which resulted in a "knock-like" abnormal combustion cycle. This issue is alleviated with the strategy proposed in the present work by using much smaller pilots, which are injected much later in the cycle to avoid overleaning of the plumes.

5.2. DICI nonpremixed hydrogen versus diesel combustion

This section compares the DICI H_2 and CDC cycles. Fig. 4 presents the injection rate, heat release rate, and pressure traces, illustrating the evolution of the combustion process. The plot is split into segments and color-coded for the former case. The following describes each phase of the DICI H_2 combustion cycle, highlighting notable distinctions to the CDC, and briefly summarizes the most important findings from our previous study [29], putting them into the context of the present work. The first phase of the DICI H_2 combustion highlighted in Fig. 4 between −5 and 0 CA° ATDC (phase I) corresponds to the *pilot ignition process*. For more details on the evolution of the pilot injection and ignition, refer to Section 5.1.

The main jet injected at TDC ignites immediately after encountering the pilot plume (also see Section 5.1). This marks the beginning of the main phase of heat release between 0 and 4 CA° ATDC, which is governed by a *free turbulent jet mixing* (phase II in Fig. 4) and occurs in a nonpremixed mode. *The free jet mixing is defined as the mixing of fuel and air induced by the jet before its collision with the piston.* The fuel–air mixing and combustion are very intense during this phase for the DICI H_2 case, causing up to 50% higher rate of heat release compared to the CDC. The share of the free jet mixing phase in the total heat release is 11 times larger with DICI H_2 combustion, which can also be seen from the more intense burning at 2 and 4 CA° after start of main injection (ASOMI) in Fig. 5.

The peripheries of the H_2 jet are also significantly hotter in this phase than with diesel, thus they are expected to make appreciable contributions to the overall burning rate, as further explained in Section 5.3.2.

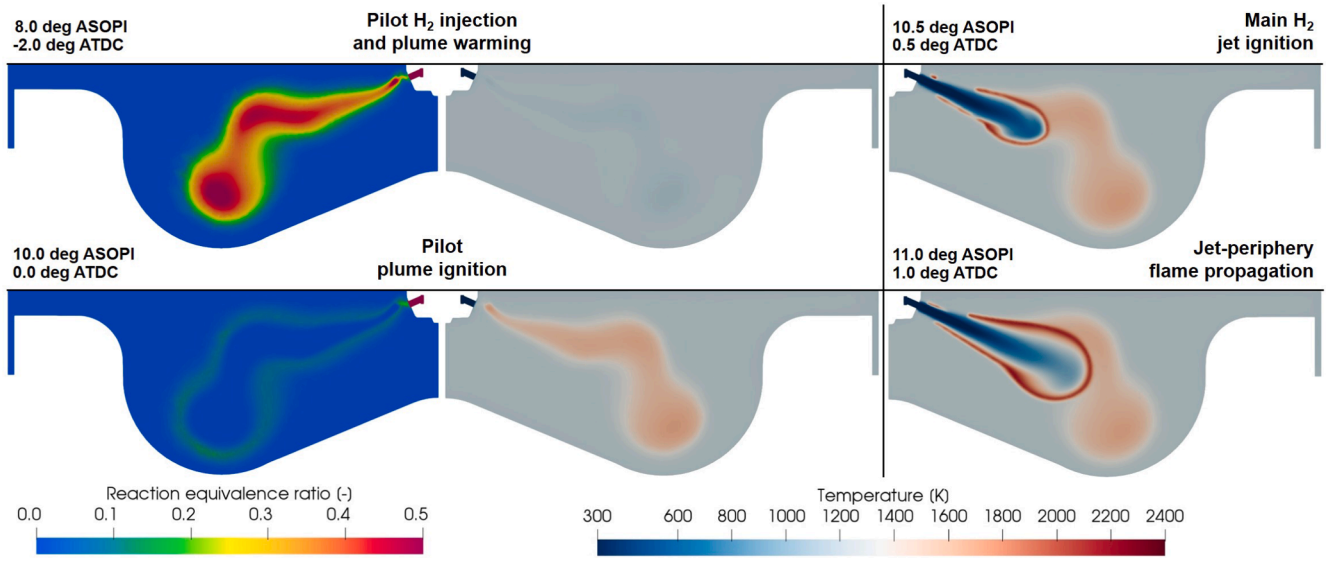

Fig. 3. Progression of a pilot H_2 injection and the subsequent main H_2 jet ignition depicted using vertical reaction equivalence ratio and temperature slices taken at the cylinder center.

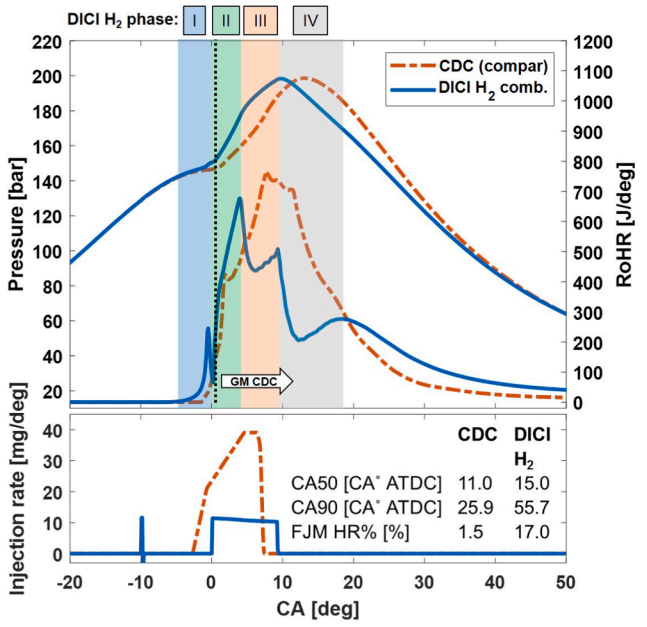

Fig. 4. Injection rate, heat release rate, pressure traces, and some combustion cycle metrics for the CDC and DICI H_2 cases. The different phases of the latter case are color-coded, while the global mixing phase of the CDC (GM CDC) is illustrated with a dotted line and an arrow. "FJM HR%" is the heat release percentage during the free jet mixing phase.

The above suggests higher effectiveness of free jet mixing with H_2, the reason for which will be explained in Section 5.3.

The *global mixing combustion* with H_2, like in conventional diesel engines, occurs during the phase of jet-piston and jet-jet interactions (phase III and IV in Fig. 4, respectively) and is associated with a drastic fall in the heat release rate, which is attributed to the reduction in the near-stoichiometric reaction region size. After the EOI at 9 CA° ATDC, the RoHR undergoes a drop before rising again and reaching another local maximum at 18 CA° ATDC. This secondary release of heat is caused by the collision of the neighboring jets and their subsequent movement back toward the cylinder center. The heat release is significantly slower with H_2 during this global mixing phase, as seen in Fig. 4 (phase IV). The reason behind that will be explained in Section 5.3.

5.3. *Fuel-air mixing in DICI H_2 combustion engines*

As described in Section 5.2, the DICI H_2 combustion is governed by two types of in-cylinder fuel–air mixing, first the free turbulent jet mixing, then the global-mixing. The heat release in the former was shown to be significantly higher with the DICI H_2 case, while the RoHR in the global mixing phase was much higher with the CDC.

To explain these results, turbulence kinetic energy (TKE) is used here as a metric to evaluate the fuel–air mixing rate in the crucial reaction region. The effectiveness of this approach is demonstrated in [54]. The TKE calculations are confined to the narrow near-stoichiometric zone ($\phi_R = 1$), where most of the combustion reactions occur. The resultant quantity is mass-averaged and presented in Fig. 6 ($\overline{TKE}_{react}$), along with the limits within which 50% and 100% of the values lie.

Two main trends must be stressed here: (1) the reaction region turbulence, and hence fuel–air mixing rate, is the highest between 0 and 3 CA° ASOMI for the DICI H_2 combustion, whereas that for the CDC is the lowest during that period; (2) the reaction region turbulence and fuel–air mixing rate for the CDC case keep increasing during the entire injection process, exceeding that for the DICI H_2 case after 4 CA° ASOMI, jet-piston collision. The physical phenomena behind the first trend are described in Sections 5.3.1, and 5.3.2, while the second trend is explained in Section 5.3.3.

5.3.1. *Injection and jet penetration velocity*

From the first two rows of Fig. 5, it is seen that the H_2 jet penetrates the chamber much faster than the diesel spray during the free-jet phase, i.e., before 4 CA° ATDC. Fig. 7 also shows the nozzle exit velocity, and consequently, the initial jet tip penetration is significantly faster for the DICI H_2 compared to the CDC case. There are several reasons for such behavior, which are discussed in the following.

First, the quasi-square injection rate profile adopted for H_2 injections contributes to the higher nozzle exit velocity. This is justified by hydrogen's low density, hence fast acceleration. Second, considering the initial pressure ratio between the H_2 injector volume and the cylinder of approximately 2:1, the discharge of H_2 gas is expected to be sonic [29]. Therefore, the H_2 gas discharging into the cylinder quickly reaches Mach 1 at around 1315 m/s (see Fig. 7), considering that H_2 has the speed of sound almost 4 times higher than that in air. This contributes to the more effective free-jet combustion with the DICI H_2 concept.

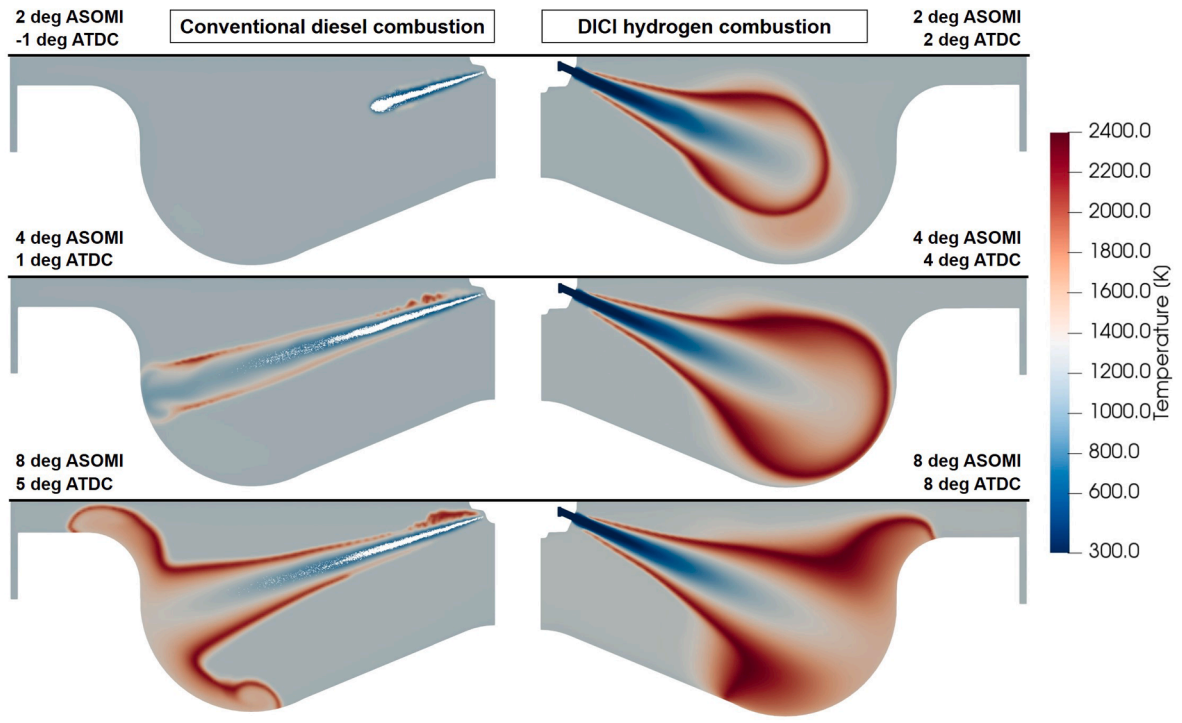

Fig. 5. Central vertical temperature slices of the cylinder, showing the progression of the main injection in the DICI H_2 and CDC (compar.) cases.

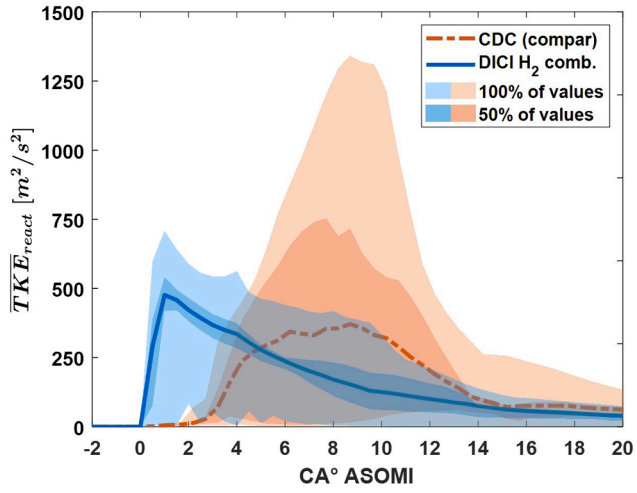

Fig. 6. Turbulence kinetic energy (TKE) of the reaction zone ($\phi_R = 1$) for the CDC and DICI H_2 combustion cases. The TKE is given in the mass-averaged form (dash-dotted lines), along with the limits where 50 % and 100 % of values lie.

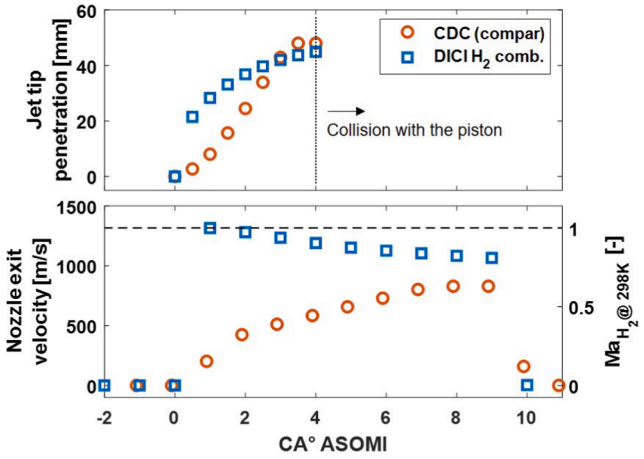

Fig. 7. Nozzle exit velocity and jet tip penetration as a function of crank angle for CDC (comparison) and DICI H_2 combustion cases.

Despite initially having a much higher velocity, the H_2 jet also slows down very quickly. This is seen from the jet tip penetration in Fig. 7, as well as from Fig. 5. This trend also matches well with the reduction in the reaction region turbulence starting from 1 CA° ATDC (Fig. 6). This is caused by hydrogen's low density, gaseous state, and faster mixing with air. The implications of the H_2 jet's quick deceleration will be further discussed in Sections 5.3.2 and 5.3.3. Note, that the lack of evaporation process with H_2 injections (unlike with diesel) also results in faster initial stages of combustion compared to the CDC, and hence, contributes to the more effective free-jet mixing.

5.3.2. *Global flow structures in DICI H_2 combustion engines*

Fig. 8 presents cylinder slices colored with reaction equivalence ratio and oriented according to the schematic in the bottom of the figure. A velocity vector field is colored with velocity magnitude and superimposed on the equivalence ratio slices. The velocity color-map range is set between 0 and 50 m/s for clear visibility of phenomena of interest. It has been shown before that non-reacting gas jets generate head vortices, and a turbulent transient gaseous jet model, known as the vortex ball model [55,56], has been widely accepted in the scientific community. In this study, recirculating flow structures or vortices generated by *reacting* H_2 jets are also observed. They are located at the periphery just behind the jet front in the so-called transient vortex region. The vortical structures and the overall width of the jet are large with H_2 due to its low density [57–59]. The flow structures inherent in H_2 injections contribute to the higher RoHR in the free-jet phase of H_2 combustion via two main mechanisms. First, the transient vortex region promotes lateral dispersion of the H_2 jet by convective transport, thus improving turbulent fuel–air mixing at its immediate location. Second, the vortices eventually create a large-scale poloidal motion of air inside the cylinder, which

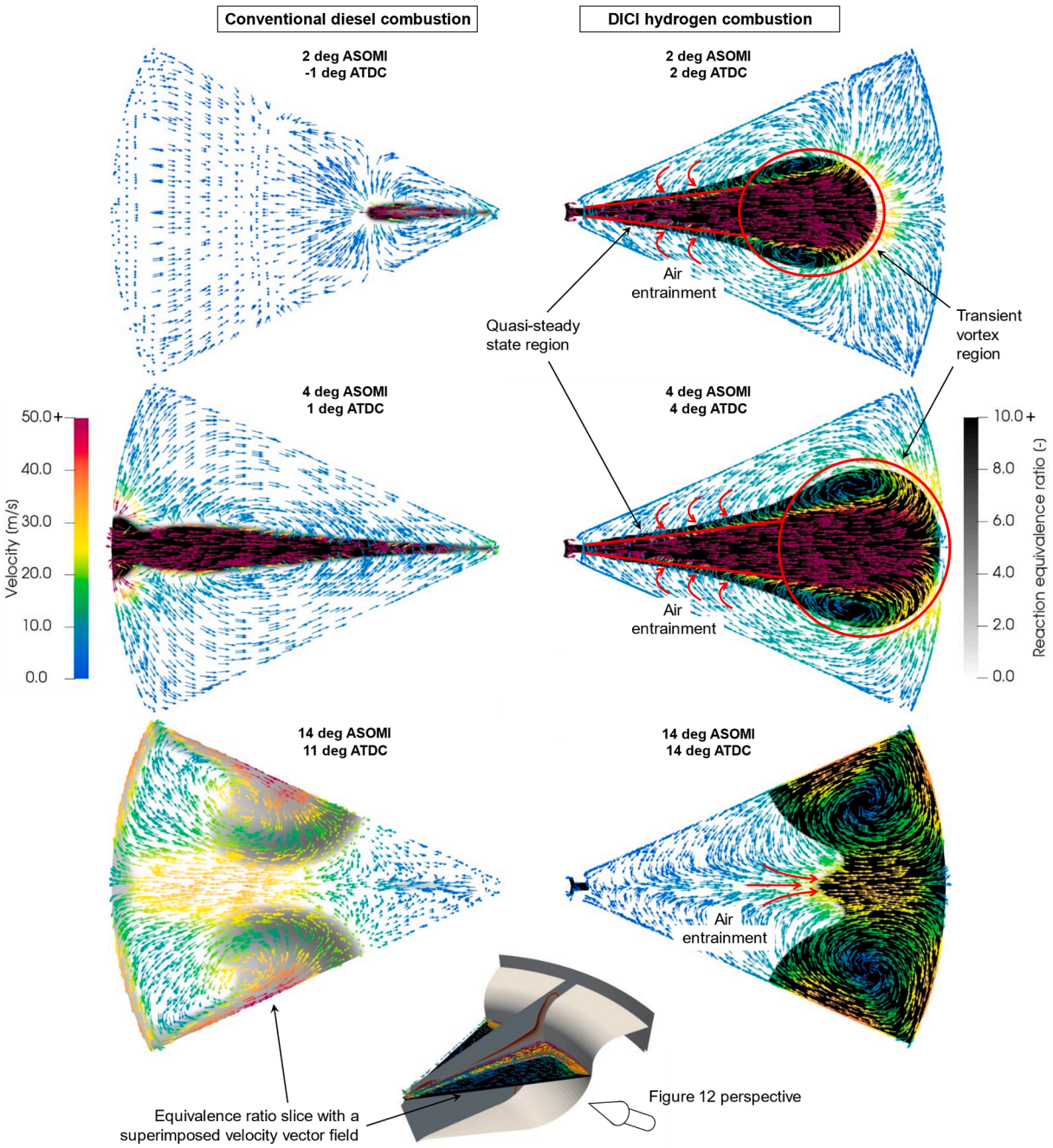

Fig. 8. Reaction equivalence ratio slices of the cylinder with superimposed velocity vector fields oriented according to the schematic in the bottom of the figure. The slices are given for the CDC and DICI H_2 combustion cases.

enhances mixing by establishing a flow of air into the portion of the jet upstream from the vortices, known as the quasi-steady-state region [56]. This is illustrated in Fig. 8 and quantified in Fig. 9. In the latter, frustum-shaped slices of the velocity vector field are applied to the quasi-steady-state regions of the H_2 and diesel jets. It is seen that the air entrainment in the former is significantly (~3 times) stronger, especially just behind the vortices.

On the other hand, the air entrainment in the diesel jets is only strong near the nozzle exit, where fuel is mostly liquid and only a few reactions occur. The fact that, in the diesel case, the fuel enters the jet near the nozzle exit unreacted, is one of the reasons behind the drastically less pronounced fuel–air stratification compared to the H_2 case. The other reason is the initially liquid state of diesel fuel. Finally, the poloidal in-cylinder motion generated by the H_2 jets persists even after the collision with the cylinder walls and EOI. It further propels the stem of the H_2 jet forward after the EOI (the last row of Fig. 8) and establishes a flow of oxidizer into the fuel-rich region in the late-cycle, thus improving the combustion efficiency.

Fig. 8 also demonstrates that the stoichiometric region is located radially further away from the jet core with H_2 combustion compared to diesel. This indicates that, unlike diesel, a significant amount of H_2 diffuses out from the jet core and partakes in reactions with O_2 not only in the vortex region but even in the quasi-steady state part of the jet. This phenomenon, combined with the higher air entrainment rate, leads to higher temperatures at the jet peripheries in the quasi-steady state regions of H_2 jets compared to diesel (Fig. 5). This is yet another reason the RoHR with H_2 combustion is higher during the free-jet mixing phase.

It should further be noted that global flow structures inherent in the

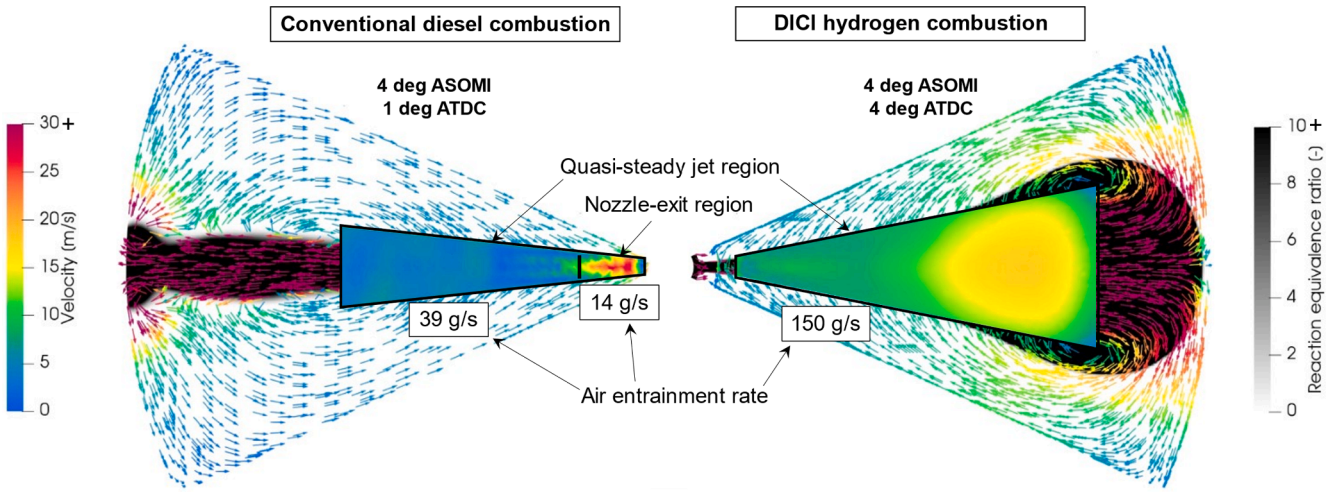

Fig. 9. Conical frustum shaped slices (top view) with side walls taken at 1 mm from the jet core and colored with velocity. The conical frustums represent the air entrainment surfaces of the jets.

DICI H_2 combustion concept not only improve the free-jet mixing but also deteriorate the global mixing phase. The wide vortex head cap causes more drag on the H_2 jet, thus slowing it down. Other reasons for the ineffective global mixing phase are elaborated in Section 5.3.3.

5.3.3. Injected and retained jet momentum

The drastic slowdown in the H_2 jet propagation, as well as the reduction in the reaction region turbulence, which are not observed with diesel jets, may be due to the following: either the injection momentum for the DICI H_2 case is low, the momentum is not effectively retained as the jet propagates, or both. The injection momentum flow rate is calculated using Eqn. (6):

$$(\dot{m}V)_e = \rho V^2 A_{in} + (P_e - P_c)A_{in} \tag{6}$$

where $(\dot{m}V)_e$ is momentum flow rate at the nozzle exit [kg-m/s^2], ρ is fluid density at the nozzle exit [kg/m^3], V is velocity at the nozzle exit [m/s], A_{in} is the nozzle exit area [m^2], P_e is the nozzle exit pressure [Pa], and P_c is mean in-cylinder pressure [Pa].

The ability of the jet to retain momentum is assessed in terms of the total jet momentum as a function of CA°, where the total jet momentum is defined as the mass of fluid parcel (computational cell) multiplied by its velocity (mV) within the hydrogen jet, that is, where $\phi_R > 1$. Fig. 10 shows the injection momentum flow rate (top) and the total jet momentum (bottom) traces for the CDC and DICI H_2 combustion concepts, along with the portion of the domain used for the jet momentum calculations. Initially, the hydrogen injection momentum flow rate is higher than that for the diesel due to the square injection rate and lack of evaporation in the former case. However, after about 2 CA° ASOMI, the diesel injection momentum exceeds that of H_2, reaching about a factor of four higher values. The total jet momentum of the DICI H_2 case is also initially higher than that of the CDC, but its rate of growth is significantly lower. After 4.7 CA° ASOMI, the momentum of the diesel jet becomes higher than that of H_2 and remains so during most of the combustion process. After the EOI, the diesel jet momentum manifests a steeper decline, which is caused by a more turbulent global mixing in that part of the cycle, as described in the beginning of Section 5.3.

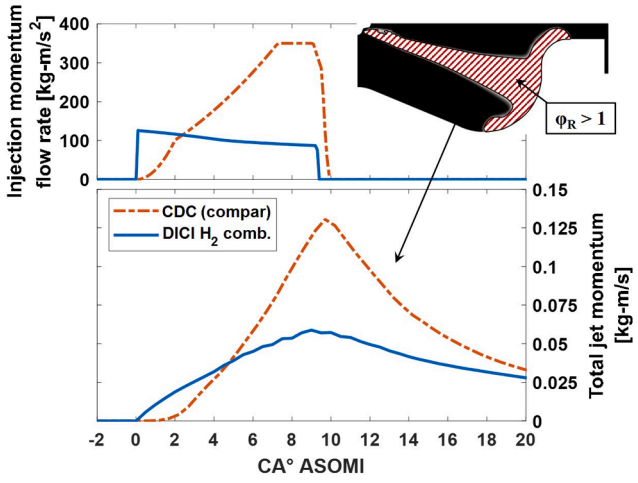

Fig. 10. Nozzle exit momentum flow rate (top) and jet momentum (bottom) for the CDC and DICI H_2 combustion cases.

Overall, both the injection momentum flow rate and the retained total jet momentum are significantly higher with the CDC compared to the DICI H_2 case during almost the entire combustion process, except for the brief period during the free-jet combustion phase. This is caused not only by the low density and relatively low injection pressure with H_2, but also the large vortex head cap of the H_2 jet that inflicts a lot of drag, as shown in Sections 5.3.1 and 5.3.2.

5.4. Thermodynamic losses and efficiency

This section discusses different sources of energy loss from the engine cylinder. The total fuel energy entering the cylinder is decomposed into four components: gross indicated work (GIW), exhaust energy, heat transfer (HT) loss, and incomplete combustion loss (from unburned fuel). Fig. 11 illustrates their relative proportions for three combustion cycles – the CDC (validation), CDC (comparison), and DICI H_2 combustion.

Note that the CDC (comparison) case is the one that was used throughout this paper for comparison with the DICI H_2 case (for details on operating conditions, refer to Section 4). All cases presented in Fig. 11 have almost equally small incomplete combustion losses; however, the remaining energy flow components vary in their proportions by a considerable amount. Heat transfer loss for the CDC (validation) only equals around 9 % of fuel energy, whereas that for the CDC (comparison) amounts to over 11 %, which is the result of overall higher in-cylinder temperatures. However, the total heat transfer loss percentage for the DICI H_2 combustion case is lower than that for both the CDC (comparison) and CDC (validation), despite having equal TDC temperatures with the former.

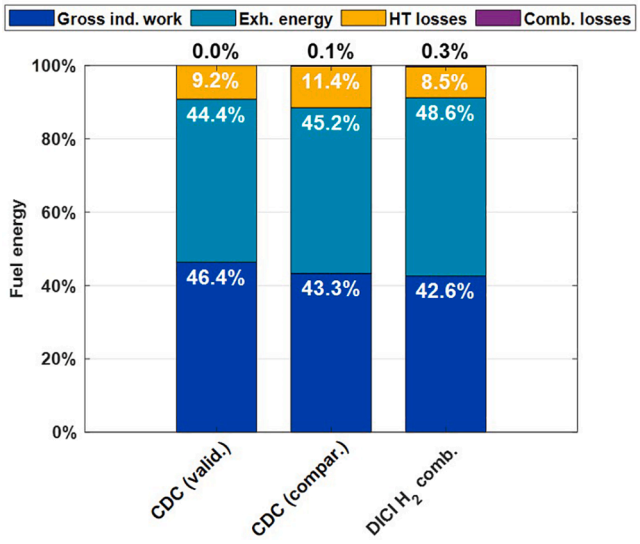

Fig. 11. Fuel energy distribution between gross indicated piston work (GIW), exhaust enthalpy, heat transfer (HT) losses, and incomplete combustion losses for different combustion cycles.

5.4.1. Wall heat transfer losses

Accumulated heat transfer losses to each combustion chamber wall (piston, head, and liner) are illustrated in Fig. 12 (left side), which shows that each component is lower with H_2 combustion. However, one particularly different component is the heat transfer to the cylinder head, which accounts for 78% of the total reduction.

Location of the heat losses. The right side of Fig. 12 shows that heat flux to the piston surface – the largest source of heat transfer losses – is the highest in the center of the jet-piston impact area and gradually reduces further away from it, both for diesel and H_2 cases. One crucial observation is that the heat flux around the flame location, i.e., peripheries of the jet impact area highlighted in white, is not significantly higher than in the surrounding areas. Overall, flame-piston heat flux (near the white contour line) is negligibly small compared to that from the jet center. Note that H_2 is known to have a short quenching distance compared to traditional hydrocarbon fuels. It is 0.64 mm at 1 bar, 298 K, and stoichiometric conditions for H_2, while that for hydrocarbon fuels is in the range of 2 mm [5]. Thus, the short quenching distance has been widely regarded as one of the factors contributing to higher heat transfer losses in SI H_2 engines [35]. However, the results of this study suggest that it does not play a significant role in nonpremixed DICI H_2 engines. These findings may also be supported by the previous research on the effects of nonreacting and reacting jet-wall impingement on heat transfer. Bovo et al. [60] demonstrated that the heat transfer coefficient dominates in the center of the nonreacting jet-wall impact area, while Song et al. [61] showed the negligible influence of reactions on the overall jet structure and their insensitivity to the presence of the wall due to a gap of several boundary layer thicknesses between them. However, the negligible effect of the quenching distance in DICI H_2 combustion remains to be confirmed in more detailed computational and experimental studies.

Thermophysical properties contributing to the heat losses. Considering that H_2 jets possess substantially less momentum (see Section 5.3.3), it seems counter-intuitive that the heat loss to the piston in the DICI H_2 case is only marginally lower than that for the CDC. Indeed, as seen in Fig. 13, the piston heat transfer rate ($\dot{Q}$) is similar with DICI H_2 and CDC cases, even though the near-piston mean velocity (v_{mean}) and temperature (T_{mean}) are in general significantly lower with the former. To demonstrate this clearly, the data is sampled at 14 CA° ATDC, where the piston heat flux and mean velocity are equal for the two cases, while the near-piston mean temperature is 309 K higher for the CDC. As a result, the convective heat transfer coefficient, defined as the heat flux (from O'Rourke and Amsden model) divided by the temperature difference, is over 50 % higher with H_2 combustion.

To explain this phenomenon, the species concentration is sampled in the center of the jet-piston impact area and presented in Table 2. The dominating species impacting the piston in the CDC case is N_2, while for the DICI H_2 case, it is H_2. After inspecting the heat transfer model in Eqns. (1)–(4), it is concluded that the thermophysical property contributing the most to the higher heat transfer coefficient with H_2 combustion is likely to be the thermal conductivity (k). This is because all other properties of H_2 on a per-mole basis would either reduce h_{conv} or not affect it significantly. The thermal conductivity of H_2, on the other hand, is seven times higher than that for N_2 (0.168 vs 0.024 W/m-K, respectively, at standard state conditions [62]).

The particularly low heat transfer loss to the cylinder head, however, is due to the low jet momentum in the DICI H_2 case (see Section 5.3.3). It requires a lot of momentum for the jet to reach the cylinder head after rebounding from the piston surface (see Fig. 5), which is very limited in the H_2 case. As a result, the flame plumes do not come into contact with the cylinder head as much as they do with the CDC, hence substantially lower heat transfer loss.

5.4.2. Efficiency

Gross indicated efficiency (GIE) is the percentage of the fuel energy converted to gross indicated work in the combustion cylinder of the DCEE. As seen in Fig. 11, the GIE of the DICI H_2 combustion cycle is lower than that of both CDC cycles. This is mainly because the combustion system used for this study is optimized for CDC, not for the H_2

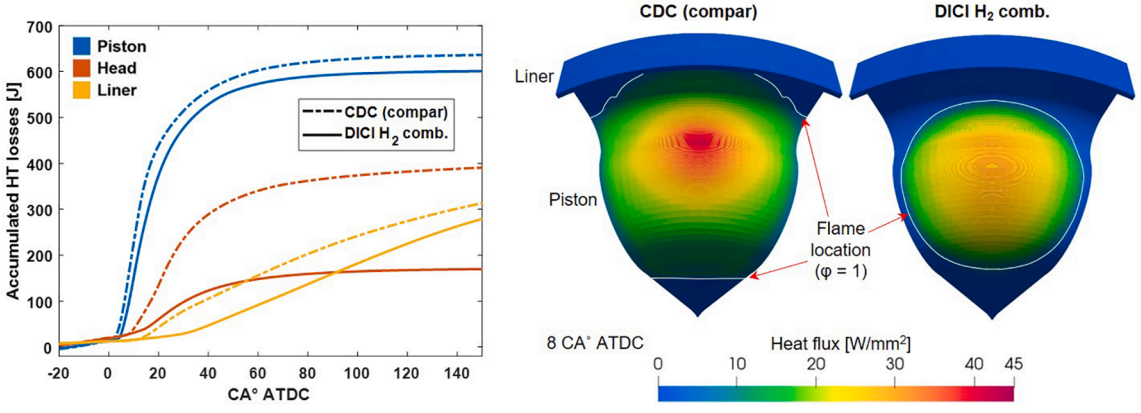

Fig. 12. Breakdown of the accumulated heat transfer losses to the combustion cylinder walls (left side), and heat flux to the piston surface (right side). The white line in the right plot is a stoichiometric *iso*-line, representing the flame location. The piston perspective is according to the bottom-most plot of Fig. 8.

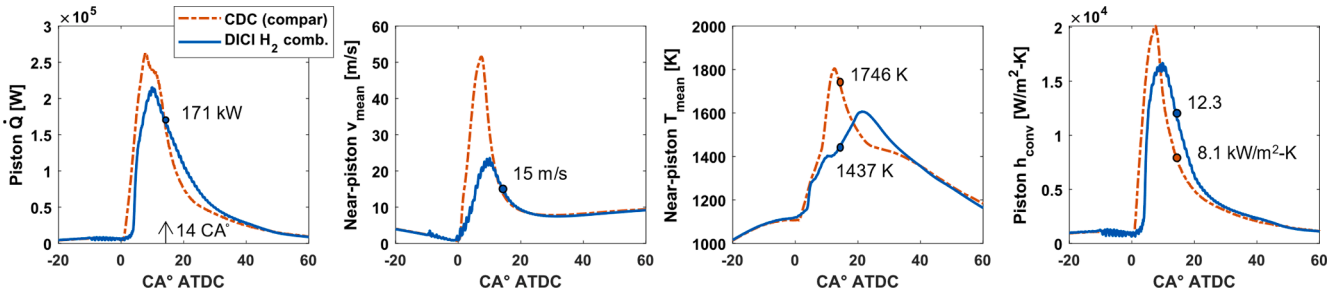

Fig. 13. Mean temperature (T_{mean}) and velocity (v_{mean}) adjacent to the piston surface, and the integrated piston heat transfer rate and convective heat transfer coefficient for the CDC and DICI H_2 combustion cases.

Table 2
Mole fractions of different species impacting the piston surface in the center of the diesel and H_2 jets.

	Fuel*	CO_2	H_2O	O_2	N_2
CDC (compar.)	< 0.001	0.089	0.132	< 0.001	0.779
DICI H_2 comb.	0.437	–	0.183	< 0.001	0.380

* Fuel for CDC is n-C_7H_{16}, while for DICI H_2 case is H_2.

concept. As a result, H_2 combustion phasing is later and duration is longer, which expectedly leads to lower efficiency. Nevertheless, owing to the considerably reduced heat transfer losses and retarded combustion phasing, the exhaust energy of the DICI H_2 combustion cycle is higher than that for both CDC cycles. In modern engine concepts, such as the DCEE, exhaust energy is used to extract additional useful work. As a result, the brake thermal efficiency (BTE) of the entire powertrain system is only marginally lower with the present implementation of the H_2 combustion concept compared to the CDC. The BTEs were estimated using a 1D GT-Power model from [32] and reported in Table 3. Note that the engine configuration used for all 1D simulations was also optimized for diesel fuel combustion. Thus, the BTE value for the DICI H_2 concept should be regarded as conservative, and prospects of further engine optimization specific to H_2 combustion should be taken into account.

Further note that, in this analysis, the H_2 fuel is assumed to be supplied from the filling stations at sufficiently high pressures so that the compression of fuel onboard of the vehicle is either not required or causes negligible losses. This assumption is justified considering that, currently, most H_2 filling stations provide fuel at 700 bar.

5.5. Potential DICI H_2 engine optimization paths

Section 5.3 explained why the global mixing phase of combustion for the DICI H_2 case showed a lower fuel–air mixing rate and sluggish heat release. Whether or not it is worthwhile attempting to improve the global mixing with H_2 combustion is an open question. Smaller injector orifice diameters will reduce the jet cap size, and consequently, the drag forces on the jet, but will simultaneously reduce its momentum. Preliminary tests have shown that the latter has a larger effect than the former, hence this strategy is unlikely to be useful. Conversely, it remains to be seen whether larger nozzle orifice diameters (above 1 mm) and higher injection pressures can significantly improve the global mixing characteristics of the DICI H_2 combustion concept. Nevertheless, achieving comparable levels of jet momentum with H_2 and diesel would lead to much higher heat transfer losses in the former case due to the high thermal conductivity of H_2 (see Section 5.4.1).

Thus, based on the findings of this work, it seems more appropriate to maximize the free-jet mixing phase of combustion with H_2 fuel, instead of pursuing the regular diesel engine optimization path of maximized global mixing. This is because, not only the fuel–air mixing and, consequently, heat release rate are higher in the free-jet phase with H_2, but also the wall heat transfer losses can be significantly reduced. Owing to the higher thermal conductivity of H_2, the lower heat transfer losses can only be guaranteed if the near-wall velocities are minimized. Additionally, pursuing free-jet mixing is expected to relax the requirements on the fuel injection system, as lower injection pressures are expected to be needed.

Practically, the DICI H_2 engine optimization path is expected to involve minimization of the contact of the H_2 jets with the piston via (1) adoption of wider piston bowl designs with shapes adapted to the H_2 jets, (2) increase in the number of injector nozzle orifices to further reduce jet-wall contact and improve in-cylinder air utilization, especially near the cylinder center, (3) reduction in the injection pressures to further reduce the jet momentum, and (4), potentially, increase of the injection rate using larger nozzle orifices to increase the amount of injected fuel before the jet-wall collision. The above should be implemented while avoiding jet-jet collapse, which might be caused by the orifices located too close to one another.

Table 3
Brake thermal efficiency (BTE) of the DCEE with the CDC (validation), CDC (comparison), and DICI H_2 combustion concepts, estimated using 1D GT-Power simulations.

	BTE of the DCEE
CDC (valid.)	53.4 %
CDC (compar.)	52.2 %
DICI H_2 comb.	53.1 %

6. Summary and conclusions

This work attempted to provide a detailed description of neat H_2 compression-ignition nonpremixed combustion and compare it with conventional diesel combustion to contribute toward the development of future carbon–neutral high-efficiency DICI H_2 engines. Closed-cycle 3D RANS simulations were performed using the CONVERGE CFD solver. The key findings of this work are summarized in the following.

1. The molar expansion work generated by the H_2 gas injection at TDC (excluding work generated by combustion) is estimated to equal 2–4 % of fuel energy or 5–10 % of the total work. It comes from a molar expansion in the nonpremixed case, which is not available with premixed H_2 combustion modes, such as SI and HCCI.
2. A small H_2 pilot injection (~1 % of the main injection) at 10 CA° before the TDC may provide a powerful ignition source, thus enabling a timely ignition of the subsequent main injection and eliminating the need for diesel pilots as in HPDI methane engines [47].
3. In contrast to conventional diesel combustion, the DICI H_2 concept is governed both by turbulent free-jet mixing and momentum-dominated global mixing. The former regime occurs before the jet-piston collision and is associated with significantly higher fuel–air mixing and burning rates with H_2.

4. The faster mixing and heat release in the free jet phase of combustion is explained by the gaseous state and low density of H_2, high injection velocity (~1300 m/s), and the global flow structures generated by the H_2 jets.
5. Reacting H_2 jets generate head vortices, which enhance fuel–air mixing via (a) promoting lateral dispersion of the jet cap and (b) creating large-scale poloidal motion of air, thus promoting entrainment into the quasi-steady-state region of the jet. Diesel jets do not exhibit such behavior to any significant extent.
6. The air entrainment into the quasi-steady-state regions of H_2 jets is around 3 times stronger than with diesel, hence heat release is also higher in those locations. In contrast, air entrainment with diesel jets dominates only near the nozzle exit, where few reactions occur. Diffusion of H_2 out from the quasi-steady state region is significant compared to diesel, also contributing to the faster heat release in the free-jet phase.
7. The ineffective global mixing with H_2 is explained by the low injected and retained jet momentum. These are due to the relatively low injection pressure (300 bar) and very low density, as well as the wide vortex head cap Redundant, hence large drag.
8. The sluggish global mixing leads to a 3 %-point reduction in heat transfer losses in the DICI H_2 engine compared to diesel. The improvements are generally due to the lower near-wall average temperatures and gas velocities. However, despite the latter, the convective heat transfer coefficient is often higher with H_2 owing to its high thermal conductivity.
9. Heat transfer modeling based on the wall-function approach suggests that the short flame quenching distance in nonpremixed CI H_2 engines may not affect heat transfer losses significantly as most of the heat flux occurs in the center of the jet-wall impact area where no reactions occur.
10. Gross indicated efficiency with the DICI H_2 combustion concept is currently up to 4 %-points lower than with conventional diesel combustion, which is attributed to larger exhaust losses. But with modern internal combustion engines capable of recovering exhaust energy, the DICI H_2 concept is expected to enable an overall system brake thermal efficiency comparable to or higher than that with the conventional diesel combustion.
11. The results of this work suggest that to optimize the engine combustion system for the DICI H_2 concept, the free-jet mixing phase should be maximized while minimizing the global mixing phase of combustion. The following are some practical recommendations that may help achieve these targets:

(a) Minimization of the contact between H_2 jets and the piston via adopting wider piston bowls with shapes adapted to the H_2 jets;
(b) Increase in the number of injector nozzle orifices;
(c) Reduction of the injection pressures;
(d) Increase in the injection rate via larger nozzle orifices.

CRediT authorship contribution statement

Rafig Babayev: Writing - original draft, Conceptualization, Methodology, Software, Validation, Formal analysis, Investigation, Visualization. **Arne Andersson:** Conceptualization, Supervision, Project administration. **Albert Serra Dalmau:** Conceptualization, Validation. **Hong G. Im:** Writing - review & editing, Funding acquisition. **Bengt Johansson:** Writing - review & editing, Supervision, Project administration, Funding acquisition.

Declaration of Competing Interest

The authors declare that they have no known competing financial interests or personal relationships that could have appeared to influence the work reported in this paper.

Acknowledgments

This work was sponsored by the King Abdullah University of Science and Technology (KAUST) and the Combustion Engine Research Center (CERC) at the Chalmers University of Technology. All simulations were performed on Shaheen II supercomputer operated by KAUST Supercomputing Laboratory (KSL). Convergent Science provided CONVERGE licenses, as well as technical support for this work.

References

[1] European Commision. A European Green Deal 2019. https://ec.europa.eu/info/strategy/priorities-2019-2024/european-green-deal_en.
[2] European Commission. EU Hydrogen Strategy 2020. https://ec.europa.eu/commission/presscorner/detail/en/fs_20_1296.
[3] European Commission. European Clean Hydrogen Alliance 2020. https://ec.europa.eu/growth/industry/policy/european-clean-hydrogen-alliance_en.
[4] Federal Ministry of Economic Affairs And Energy. The National Hydrogen Strategy 2020. https://www.bmwi.de/Redaktion/EN/Publikationen/Energie/the-national-hydrogen-strategy.html.
[5] Das LM. Hydrogen engines: a view of the past and a look into the future. Int J Hydrogen Energy 1990;15:425–43.
[6] Verhelst S, Wallner T. Hydrogen-fueled internal combustion engines. Prog Energy Combust Sci 2009;35:490–527.
[7] White CM, Steeper RR, Lutz AE. The hydrogen-fueled internal combustion engine: a technical review. Int J Hydrogen Energy 2006;31:1292–305.
[8] Antunes JMG, Mikalsen R, Roskilly AP. An investigation of hydrogen-fuelled HCCI engine performance and operation. Int J Hydrogen Energy 2008;33:5823–8.
[9] Mohammadi A, Shioji M, Nakai Y, Ishikura W, Tabo E. Performance and combustion characteristics of a direct injection SI hydrogen engine. Int J Hydrogen Energy 2007;32:296–304.
[10] Berckmüller M, Rottengruber H, Eder A, Brehm N, Elsässer G, Müller-Alander G, et al. Potentials of a charged SI-hydrogen engine. SAE Technical Paper 2003.
[11] Stenlåås O, Christensen M, Egnell R, Tunestål P, Johansson B, Mauss F. Reformed methanol gas as homogeneous charge compression ignition engine fuel. SAE Technical Paper 2004.
[12] Tsujimura T, Suzuki Y. The utilization of hydrogen in hydrogen/diesel dual fuel engine. Int J Hydrogen Energy 2017;42:14019–29.
[13] Saravanan N, Nagarajan G, Sanjay G, Dhanasekaran C, Kalaiselvan KM. Combustion analysis on a DI diesel engine with hydrogen in dual fuel mode. Fuel 2008;87:3591–9.
[14] Rao BH, Shrivastava KN, Bhakta HN. Hydrogen for dual fuel engine operation. Int J Hydrogen Energy 1983;8:381–4.
[15] SinghYadav V, Soni SL, Sharma D. Performance and emission studies of direct injection CI engine in duel fuel mode (hydrogen-diesel) with EGR. Int J Hydrogen Energy 2012;37:3807–17.
[16] Rottengruber H. Investigation of a direct injection hydrogen diesel-engine. Hydrog Energy Prog XII 1998;2:1515.
[17] Aleiferis PG, Rosati MF. Controlled autoignition of hydrogen in a direct-injection optical engine. Combust Flame 2012;159:2500–15.
[18] Lee S, Kim G, Bae C. Lean combustion of stratified hydrogen in a constant volume chamber. Fuel 2021;301:121045.
[19] Yu X, Guo Z, He L, Dong W, Sun P, Du Y, et al. Experimental study on lean-burn characteristics of an SI engine with hydrogen/gasoline combined injection and EGR. Int J Hydrogen Energy 2019;44:13988–98. Doi: 10.1016/j.ijhydene.2019.03.236.
[20] Ma F, Wang Y, Liu H, Li Y, Wang J, Zhao S. Experimental study on thermal efficiency and emission characteristics of a lean burn hydrogen enriched natural gas engine. Int J Hydrogen Energy 2007;32:5067–75. Doi: 10.1016/j.ijhydene.2007.07.048.
[21] Ji C, Wang S. Experimental study on combustion and emissions performance of a hybrid hydrogen–gasoline engine at lean burn limits. Int J Hydrogen Energy 2010;35:1453–62. Doi: 10.1016/j.ijhydene.2009.11.051.
[22] Ikegami M, Miwa K, Shioji M. A study of hydrogen fuelled compression ignition engines. Int J Hydrogen Energy 1982;7:341–53.
[23] Furuhama S, Fukuma T. High output power hydrogen engine with high pressure fuel injection, hot surface ignition and turbocharging. Int J Hydrogen Energy 1986;11:399–407.
[24] Naber JD, Siebers DL. Hydrogen combustion under diesel engine conditions. Int J Hydrogen Energy 1998;23:363–71.
[25] Eichlseder H, Spuller C, Heindl R, Gerbig F, Heller K. Konzepte für die dieselähnliche Wasserstoffverbrennung. MTZ-Motortechnische Zeitschrift 2010;71:60–6.
[26] Kavtaradze RZ. Improving the ecological indices of a hydrogen diesel engine with direct gaseous hydrogen injection. J Mach Manuf Reliab 2016;45:307–15.
[27] Natriashvili T, Kavtaradze R, Glonti M. Improvement of ecological characteristics of the hydrogen diesel engine. IOP Conf. Ser. Mater. Sci. Eng., vol. 315, IOP Publishing; 2018, p. 12018.
[28] Kavtaradze R, Natriashvili T, Gladyshev S. Hydrogen-Diesel engine: Problems and prospects of improving the working process. SAE Technical Paper 2019.
[29] Babayev R, Andersson A, Dalmau AS, Im HG, Johansson B. Computational characterization of hydrogen direct injection and nonpremixed combustion in a compression-ignition engine. Int J Hydrogen Energy 2021.

[30] Lam N, Tuner M, Tunestal P, Andersson A, Lundgren S, Johansson B. Double compression expansion engine concepts: a path to high efficiency. SAE Int J Engines 2015;8:1562–78.
[31] Lam N, Andersson A, Tunestal P. Double Compression Expansion Engine Concepts: Efficiency Analysis over a Load Range. SAE Technical Paper 2018.
[32] Lam N, Tunestal P, Andersson A. Simulation of System Brake Efficiency in a Double Compression-Expansion Engine-Concept (DCEE) Based on Experimental Combustion Data. SAE Technical Paper 2019.
[33] Shankar VSB, Lam N, Andersson A, Johansson B. Optimum heat release rates for a double compression expansion (DCEE) engine. SAE Technical Paper 2017.
[34] Lam N. Double Compression-Expansion Engine Concepts: Experimental and simulation study of a split-cycle concept for improved brake efficiency. Lund University; 2019.
[35] Yip HL, Srna A, Yuen ACY, Kook S, Taylor RA, Yeoh GH, et al. A Review of Hydrogen Direct Injection for Internal Combustion Engines: Towards Carbon-Free Combustion. Appl Sci 2019;9:4842.
[36] Yamane K. Hydrogen Fueled ICE, Successfully Overcoming Challenges through High Pressure Direct Injection Technologies: 40 Years of Japanese Hydrogen ICE Research and Development. SAE Technical Paper 2018.
[37] Nguyen D-K, Szybist J, Sileghem L, Verhelst S. Effects of molar expansion ratio of fuels on engine efficiency. Fuel 2020;263:116743. Doi: 10.1016/j.fuel.2019.116743.
[38] Date AW. Analytic Combustion. Springer; 2011.
[39] Johansson B. Combustion engines. Department of Energy Sciences. Lund University; 2014.
[40] Richards KJ, Senecal PK, Pomraning E. CONVERGE 3.0. Converg Sci Madison, WI; 2000.
[41] Amsden AA, Findley M. KIVA-3V: A block-structured KIVA program for engines with vertical or canted valves. Lawrence Livermore National Lab.(LLNL), Livermore, CA (United States); 1997.
[42] Nasrifar K. Comparative study of eleven equations of state in predicting the thermodynamic properties of hydrogen. Int J Hydrogen Energy 2010;35:3802–11.
[43] Richards, K. J., Senecal, P. K., and Pomraning, E., CONVERGE 3.0 Manual, Convergent Science, Madison, WI (2020). n.d.
[44] Smith GP, Golden DM, Frenklach M, Moriarty NW, Eiteneer B, Goldenberg M, et al. GRI-Mech 3.0 n.d. http://combustion.berkeley.edu/gri-mech/version30/text30.html.
[45] Smith GP, Tao Y, Wang H. Foundation Fuel Chemistry Model Version 1.0 (FFCM-1) 2016. http://nanoenergy.stanford.edu/ffcm1.
[46] Wang H, You X, Joshi A V., Davis SG, Laskin A, Egolfopoulos F, et al. USC Mech Version II. High-Temperature Combustion Reaction Model of H2/CO/C1-C4 Compounds 2007. http://ignis.usc.edu/USC_Mech_II.htm.
[47] McTaggart-Cowan G, Mann K, Huang J, Singh A, Patychuk B, Zheng ZX, et al. Direct injection of natural gas at up to 600 bar in a pilot-ignited heavy-duty engine. SAE Int J Engines 2015;8:981–96.
[48] Burke MP, Chaos M, Ju Y, Dryer FL, Klippenstein SJ. Comprehensive H2/O2 kinetic model for high-pressure combustion. Int J Chem Kinet 2012;44:444–74.
[49] Sarathy M, Atef N, Alfazazi A, Badra J, Zhang Y, Tzanetakis T, et al. Reduced gasoline surrogate (toluene/n-heptane/iso-octane) chemical kinetic model for compression ignition simulations. SAE Technical Paper 2018.
[50] Boretti A. Advances in Diesel-LNG internal combustion engines. Appl Sci 2020;10:1296.
[51] Liu J, Yang F, Wang H, Ouyang M, Hao S. Effects of pilot fuel quantity on the emissions characteristics of a CNG/diesel dual fuel engine with optimized pilot injection timing. Appl Energy 2013;110:201–6.
[52] Ryu K. Effects of pilot injection timing on the combustion and emissions characteristics in a diesel engine using biodiesel–CNG dual fuel. Appl Energy 2013;111:721–30.
[53] Sudarmanta B, Setiyawan A, Putra ABK, Yuvenda D, Silva JD. Optimization of pilot diesel injection timing on load variation dual fuel diesel-CNG engine on combustions and emissions characteristics. Int Rev. Mech Eng 2019;13.
[54] Eismark J, Hammas M, Karlsson A, Denbratt I, Davidson L. Role of turbulence for mixing and soot oxidation for an equivalent diesel gas jet during wall interaction studied with LES. THIESEL 2012 Conf. Thermo-and Fluid Dyn. Process. Direct Inject. Engines, Citeseer; 2012, p. 1–16.
[55] Turner JS. The 'starting plume' in neutral surroundings. J Fluid Mech 1962;13:356–68.
[56] Ouellette P. Direct injection of natural gas for diesel engine fueling. University of British Columbia; 1996.
[57] Amielh M, Djeridane T, Anselmet F, Fulachier L. Velocity near-field of variable density turbulent jets. Int J Heat Mass Transf 1996;39:2149–64.
[58] Shahsavan M, Morovatiyan M, Mack JH. A numerical investigation of hydrogen injection into noble gas working fluids. Int J Hydrogen Energy 2018;43:13575–82.
[59] Maxwell B, Oshkai P, Djilali N. Experimental and numerical investigation of turbulent jets issuing through a realistic pipeline geometry: Asymmetry effects for air, helium, and hydrogen. Int J Hydrogen Energy 2018;43:9379–98.
[60] Bovo M, Rojo B. Single pulse jet impingement on inclined surface, heat transfer and flow field. SAE Technical Paper 2013.
[61] Song L, Abraham J. Influence of wall impingement on the structure of reacting jets. SAE Technical Paper 2003.
[62] Engineering ToolBox. Thermal Conductivity - selected Materials and Gases 2003. https://www.engineeringtoolbox.com/thermal-conductivity-d_429.html.